Scientific Research Publishing

Advances in Materials Physics and Chemistry, 2022, 12, 33-45
https://www.scirp.org/journal/ampc
ISSN Online: 2162-5328
ISSN Print: 2162-531X

Tunable Optical Bandgap of Gadolinium Substituted Nickel-Zinc Ferrite Nanoparticles-Effect of Calcination Temperature on Its Optical Parameters

Katrapally Vijaya Kumar

Department of Physics, JNTUH University College of Engineering, Rajanna Sircilla, India
Email: kvkphd@gmail.com, kvkumar@jntuh.ac.in

How to cite this paper: Kumar, K.V. (2022) Tunable Optical Bandgap of Gadolinium Substituted Nickel-Zinc Ferrite Nanoparticles-Effect of Calcination Temperature on Its Optical Parameters. *Advances in Materials Physics and Chemistry*, **12**, 33-45.
https://doi.org/10.4236/ampc.2022.123003

Received: February 26, 2022
Accepted: March 28, 2022
Published: March 31, 2022

Copyright © 2022 by author(s) and Scientific Research Publishing Inc.
This work is licensed under the Creative Commons Attribution International License (CC BY 4.0).
http://creativecommons.org/licenses/by/4.0/

Open Access

Abstract

The gadolinium substituted nickel-zinc ferrite nanoparticles of the composition, $Ni_{0.5}Zn_{0.5}Gd_{0.05}Fe_{1.95}O_4$ were prepared using sol-gel method. In order to study the effect of calcination temperature on the optical parameters, the prepared powder was divided into five parts. The first part was taken as the as-prepared sample and the remaining four parts were calcinated at different temperatures, 600˚C, 700˚C, 800˚C & 900˚C. The X-ray diffraction patterns revealed the formation of cubic spinel structure with single phase and Fd3m space group. The crystallite size was increased from 11.75 nm to 18.13 nm as the calcination temperature increased from 600 to 900˚C whereas as-prepared sample exhibited 17.61 nm. The dislocation density was decreased from 7.243 × 10^{-3} to 3.042 × 10^{-3} nm^{-2} as the calcination temperature increased from 600˚C to 900˚C. The micro strain was decreased from 10 × 10^{-4} to 6.452 × 10^{-4} as the calcination temperature increased from 600˚C to 900˚C. The characteristic absorbance peaks were obtained at 255.2 nm for the ferrite nanoparticles of as-prepared and calcinated at 600˚C and 800˚C whereas it was obtained as 252.8 nm for the sample calcinated at 700˚C and there was no such characteristic peak in UV-visible range for the sample calcinated at 900˚C; it is expected in the below 200 nm region. The optical energy gap was calculated using Kubelka-Munk equation based on Tauc's plot and found in the range 4.100 eV to 5.389 eV. The lowest energy gap of 4.100 eV exhibited by the sample calcinated at 700˚C and the highest energy gap of 5.389 eV by the sample calcinated at 900˚C. It is concluded that the tunable band gaps can be obtained with varying calcination temperature.

Keywords

XRD, Optical Energy Bandgap, Refractive Index, Absorption Coefficient,

Extinction Coefficient, Real and Imaginary Parts of Dielectric Constant

1. Introduction

Ferrites are known as the magnetic materials having cubic spinel structure with chemical formula AB_2O_4, where "A" indicates the divalent cations such as Mg^{2+}, Ni^{2+}, Cu^{2+}, Co^{2+}, Zn^{2+}, and "B" indicates the trivalent metal ion of Fe^{3+} [1]. In fact, bulk and ferrites nanoparticles perform widespread applications in various manufacturing and scientific fields. Predominantly, these materials reveal more important in memory devices such as magnetic tapes and hard disk devices, and in the field of biomedicine, these were used as magnetic hyperthermia, magnetic resonance imaging (MRI) application. In the field of communication systems, these are used as transformer & inductor core devices, electromagnetic shielding, multilayer chip inductors (MLCIs), high-frequency antenna devices, humidity & temperature sensors, magnetic refrigeration [2]. The applications of ferrite nanoparticles are also extended in the disciplines such as biomedical technology [3], nuclear magnetic resonance [4], magnetic fluid [5], hydroelectric energy [6], optoelectronic sensor [7], and catalyst [8]. Further, the applications of these materials in industry are due to their promising dielectric and opto-electronic properties [9] [10] [11] [12]. The dielectric and opto-electronic characteristics of these materials are highly relied on the crystal structure, existence of various metal ions in crystal structure, nature and quantity of substitution or dopant.

UV-vis absorption spectra have been used to investigate the band gap energies of AB_2O_4 spinel ferrites [13]-[18]. Jariti Pal *et al.* studied the characteristics of Co_3O_4 nanocrystals, and gave curves of $(\alpha h\nu)^2$ vs $h\nu$, where α is the UV-vis absorption coefficient, and $h\nu$ is the photon energy. Using this curve, they obtained two optical energy bandgaps, 2.28 and 1.57 eV. They appealed that the two optical energy band gaps link to the electron transitions for O^{2-} to Co^{2+} and O^{2-} to Co^{3+}, respectively [13]. In the similar manner, Hu *et al.* studied the properties of $NiCo_2O_4$ nanoparticles and observed two optical energy bandgaps, 2.0 eV and 3.3 eV, which were attributed to the co-existence of high-spin and low-spin states of Co^{3+} in the $NiCo_2O_4$ spinel [14]. Cui *et al.* estimated the optical energy bandgaps from O 2p to Co 3d-e_g and Co 3d-t_{2g} for ordinary $NiCo_2O_4$, and found values of 3.40 and 1.97 eV, respectively [15]. Melsheimer *et al.* studied the band gap energies of heteropoly compounds using differential UV absorption spectra, dα/dE vs E, where $E = h\nu$ is the photon energy [18]. In the present study, apart from the analysis of the effect of calcination temperature on optical energy bandgaps, a sincere effort was put forward to analyze the effect of calcination temperature on several optical parameters, such as, refractive index, absorption coefficient, extinction coefficient, real and imaginary parts of dielectric constant, as no one focused on such study of $Ni_{0.5}Zn_{0.5}Gd_{0.05}Fe_{1.95}O_4$ nanoparticles. This is really significant in understanding magnetic properties and electrical transport of a

material.

2. Materials

Ferrite nanoparticles of the composition, $Ni_{0.5}Zn_{0.5}Gd_{0.05}Fe_{1.95}O_4$ were prepared by sol-gel method [19]. Nickel nitrate, zinc nitrate, iron nitrate, gadolinium nitrate, citric acid and ammonia of analytical grade were used as starting materials. Using the materials, nickel nitrate ($Ni(NO_3)_2{\cdot}6H_2O$), ferric nitrate ($Fe(NO_3)_3{\cdot}9H_2O$), zinc nitrate ($Zn(NO_3)_2{\cdot}6H_2O$) and gadolinium nitrate ($Gd(NO_3)_3$), a solution was prepared in their stoichiometry and dissolved in a de-ionized water. With the addition of citric acid, the prepared aqueous solution was made to chelate Ni^{2+}, Zn^{2+}, Gd^{3+} and Fe^{3+} ions in the solution. The molar ratio was adjusted to 1:3 ratio between the citric acid and total moles of nitrate ions. The pH value of mixed solution was maintained at 7 by neutralizing the solution with the ammonia (NH_3) in adequate proportion. The neutralized solution was heated at about 100˚C on a hot plate with continuous stirring to get final product in the form of viscous gel. The temperature was increased to about 300˚C and led to ignite the formed gel and burnt completely in a self-propagating combustion manner to form a loose powder [20] [21]. The prepared powder is divided into five parts, one part was kept away from calcination and just treated as as-prepared sample and the remaining four parts were calcinated at 600˚C, 700˚C, 800˚C & 900˚C for 8 h.

3. Results and Discussions

The XRD patterns of all the samples have been recorded at room temperature using Shimadzu XRD-7000 X-Ray Diffractometer are presented in **Figure 1**. They exhibited cubic spinel structure with single phase and Fd3m space group. The XRD data were fitted using the X' Pert High Score Plus software with the Rietveld powder diffraction profile fitting technique [22]. In **Table 1**, the

Table 1. Lattice parameters, Bragg's angle, FWHM, crystallite size, density, microstrain and Energy gap of $Ni_{0.5}Zn_{0.5}Gd_{0.05}Fe_{1.95}O_4$ ferrite nanoparticles (as-prepared and calcinated at 600˚C, 700˚C, 800˚C & 900˚C).

Calcination Temperature	As-Prepared	600˚C	700˚C	800˚C	900˚C
Lattice Parameter (a) (Å)	8.389	8.382	8.373	8.367	8.360
Volume of Unit Cell (Å^3)	590.38	588.90	587.01	585.75	584.28
Bragg's Angle (2θ) (˚)	35.58	35.76	35.65	35.49	35.62
FWHM (˚)	0.47386	0.71047	0.64333	0.5778	0.46028
X-ray Density (ρ_x) (g/cm^3)	4037	4107	4120	4129	4140
Crystallite Size (D) (nm)	17.61	11.75	12.98	14.44	18.13
Dislocation Density (δ_D) (nm^{-2}) × 10^{-3}	3.225	7.243	5.935	4.796	3.042
Microstrain (ε) × 10^{-4}	6.634	10.000	9.0260	8.068	6.452
Absorbance peak (λ_{max}) (nm)	255.2	255.2	252.8	255.2	-
Energy Gap (E) (eV)	4.327	4.266	4.100	4.308	5.389

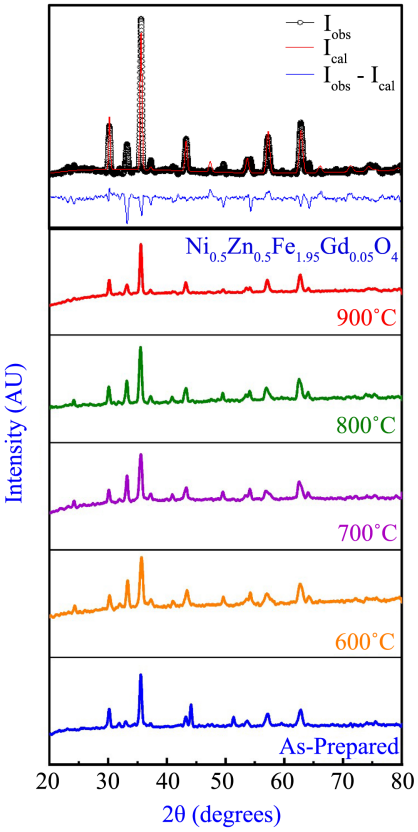

Figure 1. X-ray diffraction patterns of $Ni_{0.5}Zn_{0.5}Gd_{0.05}Fe_{1.95}O_4$ ferrite nanoparticles (as-prepared and calcinated at 600˚C, 700˚C, 800˚C & 900˚C) [22].

parameters such as lattice parameters, Bragg's angle, FWHM, crystallite size, dislocation density and micro strain of all the samples are furnished. The addition of gadolinium ions increases the micro strain (ε) in nickel-zinc ferrite nanoparticles, because the gadolinium ion radius is greater than the ferric ion radius. The micro strain value can be calculated from Equation (1) [23].

$$\varepsilon = \frac{\beta}{4\tan\theta} \tag{1}$$

The micro strain value decreased from 10×10^{-4} to 6.452×10^{-4} as the calcination temperature increases from 600˚C to 900˚C whereas the as-prepared sample has a value of 6.634×10^{-4}. The dislocation density (δ_D) is inversely proportional to the square of crystallite size. The dislocation density increases with the defect occurrence due to any kind of reason and it can be calculated from the following Equation (2) [23]

$$\delta_D = \frac{1}{D^2} \tag{2}$$

The density of dislocation was decreased from 7.243×10^{-3} to 3.042×10^{-3} nm^{-2} as the calcination temperature increases from 600˚C to 900˚C whereas the as-prepared sample has a value of 3.225×10^{-3} nm^{-2}. It is clearly noticed that there was a systematic effect of calcination temperature on micro strain and dis-

location density of taken up samples. The X-ray density in the cubic system can be calculated from the following Equation (3) [24].

$$\rho_x = \frac{ZM}{NV} \tag{3}$$

where, $Z = 8$ for a cubic system (Unit formula), M is the molecular weight of ferrite, N the Avogadro's number (6.023×10^{23} mol^{-1}) and V is the volume of cell unit. The X-ray density was increased from 4037 to 4140 g/cm^3 as calcination temperature increases from as-prepared sample to 900˚C.

The UV-visible absorption spectra of all the samples were measured with a spectrophotometer (SYSTRONICS DOUBLE BEAM UV-Vis Spectrometer: 2202) at room temperature in the wavelength range 200 - 800 nm, with a maximum step size of 0.2 nm. The absorbance can be obtained from the instrument and the transmittance can be calculated using the following relation (4).

$$T_s = 10^{-A} \times 100 \tag{4}$$

where, T_s is known as transmittance and A is known as Absorbance. Hence, the absorption coefficient can be calculated using the following relation (5) [25].

$$\alpha = \frac{2.303 \times A}{l} \tag{5}$$

where, α is known as absorption coefficient, A is known as absorbance and l is known as thickness of the specimen. **Figure 2** shows the variation of absorbance and transmittance of all the ferrite nanoparticles (as-prepared and calcinated at 600˚C, 700˚C, 800˚C & 900˚C) with wavelength in UV-visible range, 200 - 800 nm. In the case of U. Naresh, *et al.*, for $CuFe_2O_4$ the characteristic absorbance peak was obtained in the range 311 - 340 nm [26]. The characteristic absorbance peaks were obtained at 255.2 nm for the ferrite nanoparticles of as-prepared and calcinated at 600˚C and 800˚C whereas it was obtained as 252.8 nm for the sample calcinated at 700˚C and there was no such characteristic peak in UV-visible range for the sample calcinated at 900˚C, may be the it would be in the below

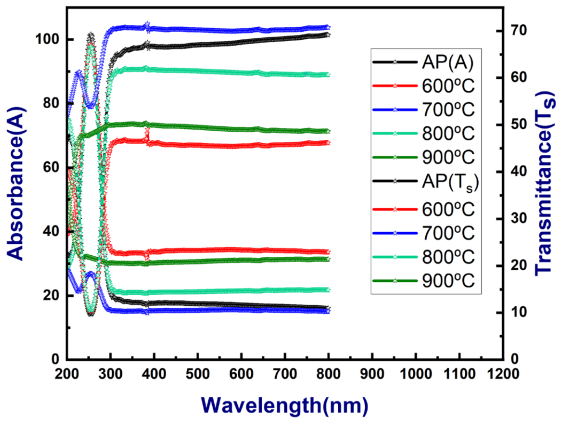

Figure 2. Variation of absorbance and transmittance of $Ni_{0.5}Zn_{0.5}Gd_{0.05}Fe_{1.95}O_4$ ferrite nanoparticles (as-prepared and calcinated at 600˚C, 700˚C, 800˚C & 900˚C) with wavelength in UV-Visible region.

200 nm region. The refractive index can be measured with the help of following relation (6).

$$n = \frac{1}{T_s} + \sqrt{\frac{1}{T_s - 1}} \tag{6}$$

where, n is refractive index and T_s is transmittance. Figure 3 shows the variation of refractive index of $Ni_{0.5}Zn_{0.5}Gd_{0.05}Fe_{1.95}O_4$ ferrite nanoparticles (as-prepared and calcinated at 600˚C, 700˚C, 800˚C & 900˚C) with wavelength in UV-visible region, 200 - 800 nm. From the study, it was observed clearly that refractive index of the samples increased gradually, reaches maximum and then decreased. The characteristic peaks were observed at the characteristic wavelengths observed for absorbance peaks. Using the following relation (7), extinction coefficient can be calculated [27].

$$k = \frac{\alpha\lambda}{4\pi} \tag{7}$$

where, k is extinction coefficient, λ is wavelength and α is absorption coefficient. Figure 4 shows the variation of extinction coefficient of $Ni_{0.5}Zn_{0.5}Gd_{0.05}Fe_{1.95}O_4$ ferrite nanoparticles (as-prepared and calcinated at 600˚C, 700˚C, 800˚C & 900˚C) with wavelength in UV-visible region, 200 - 800 nm. All the samples exhibited a characteristic peak except the sample calcinated at 900˚C. In case of all the samples, the extinction coefficient was gradually increased, reached maximum and then decreased in the wavelength range, 200 to 300 nm, there onwards, the extinction coefficient increased linearly except the case of sample calcinated at 900˚C. In case of sample calcinated at 900˚C, the extinction coefficient varied linearly from 200 to 800 nm, may be the characteristic peak would be in the below 200 nm region. It was clearly observed that extinction coefficient was observed maximum for the as-prepared sample and it was observed low for the sample calcinated at 700˚C.

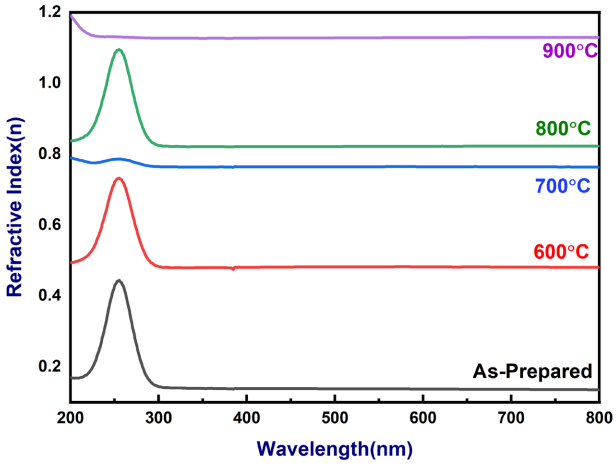

Figure 3. Variation of refractive index of $Ni_{0.5}Zn_{0.5}Gd_{0.05}Fe_{1.95}O_4$ ferrite nanoparticles (as-prepared and calcinated at 600˚C, 700˚C, 800˚C & 900˚C) with wavelength in UV-Visible region.

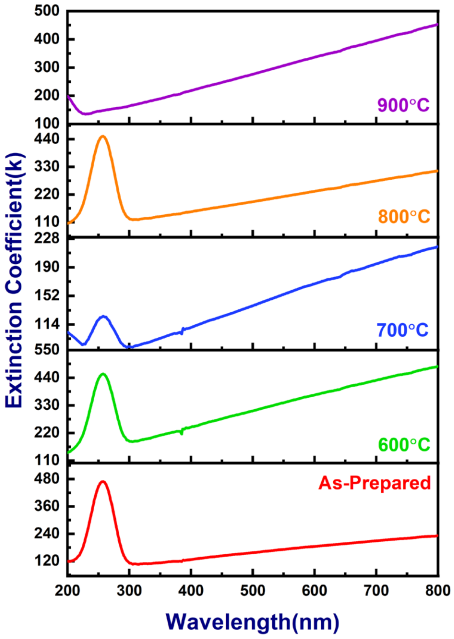

Figure 4. Variation of extinction coefficient of $Ni_{0.5}Zn_{0.5}Gd_{0.05}Fe_{1.95}O_4$ ferrite nanoparticles (as-prepared and calcinated at 600˚C, 700˚C, 800˚C & 900˚C) with wavelength in UV-Visible region.

The reflectance can be calculated with the help of refractive index, as follows (8) [28]:

$$R = \frac{(n-1)^2}{(n+1)^2} \tag{8}$$

where, R is reflectance, and n is refractive index. **Figure 5** shows the variation of reflectance of $Ni_{0.5}Zn_{0.5}Gd_{0.05}Fe_{1.95}O_4$ ferrite nanoparticles (as-prepared and calcinated at 600˚C, 700˚C, 800˚C & 900˚C) with wavelength in UV-visible region, 200 - 800 nm. All the samples exhibited a characteristic peak except the sample calcinated at 900˚C. In case of all the samples, the extinction coefficient was gradually decreased, reached minimum and then increased in the wavelength range, 200 to 300 nm, there onwards, the reflectance was constant except the case of sample calcinated at 900˚C. In case of sample calcinated at 900˚C, the reflectance increased gradually till 300 nm and there onwards it was consistent, may be the characteristic peak would be in the below 200 nm region. It was clearly observed that the reflectance was observed maximum for the as-prepared sample and reflectance was observed low for the sample calcinated at 600˚C.

Using the refractive index and extinction coefficient, the real and imaginary parts of dielectric constant can be expressed with the following relations (9 and10) [29] [30].

$$\varepsilon_i = 2nk \tag{9}$$

$$\varepsilon_r = n^2 - k^2 \tag{10}$$

Figure 6 shows the variation of real and imaginary parts of dielectric constant of $Ni_{0.5}Zn_{0.5}Gd_{0.05}Fe_{1.95}O_4$ ferrite nanoparticles (as-prepared and calcinated at

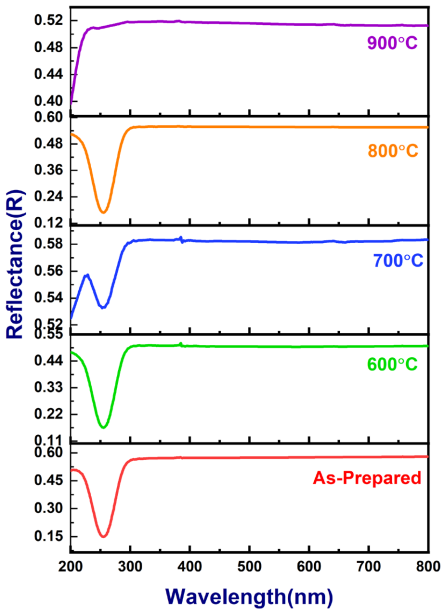

Figure 5. Variation of reflectance of $Ni_{0.5}Zn_{0.5}Gd_{0.05}Fe_{1.95}O_4$ ferrite nanoparticles (as-prepared and calcinated at 600˚C, 700˚C, 800˚C & 900˚C) with wavelength in UV-Visible region.

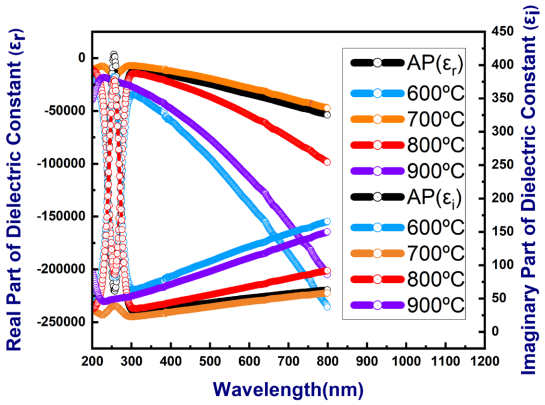

Figure 6. Variation of real and imaginary parts of dielectric constant of $Ni_{0.5}Zn_{0.5}Gd_{0.05}Fe_{1.95}O_4$ ferrite nanoparticles (as-prepared and calcinated at 600˚C, 700˚C, 800˚C & 900˚C) with wavelength in UV-Visible region.

600˚C, 700˚C, 800˚C & 900˚C) with wavelength in UV-Visible region, 200 - 800 nm. All the samples exhibited a characteristic peak except the sample calcinated at 900˚C, may be the characteristic peak would be in the below 200 nm region.

The optical energy bandgap (E_g) of $Ni_{0.5}Zn_{0.5}Gd_{0.05}Fe_{1.95}O_4$ ferrite nanoparticles (as-prepared and calcinated at 600˚C, 700˚C, 800˚C & 900˚C) were calculated using the Tauc plots. The absorption coefficient of the ferrite nanoparticles has been determined from the absorption data by using the fundamental relationships (11, 12 and 13) [31] [32].

$$I = I_0 e^{\alpha t} \tag{11}$$

$$A = \log \frac{I_0}{I} \tag{12}$$

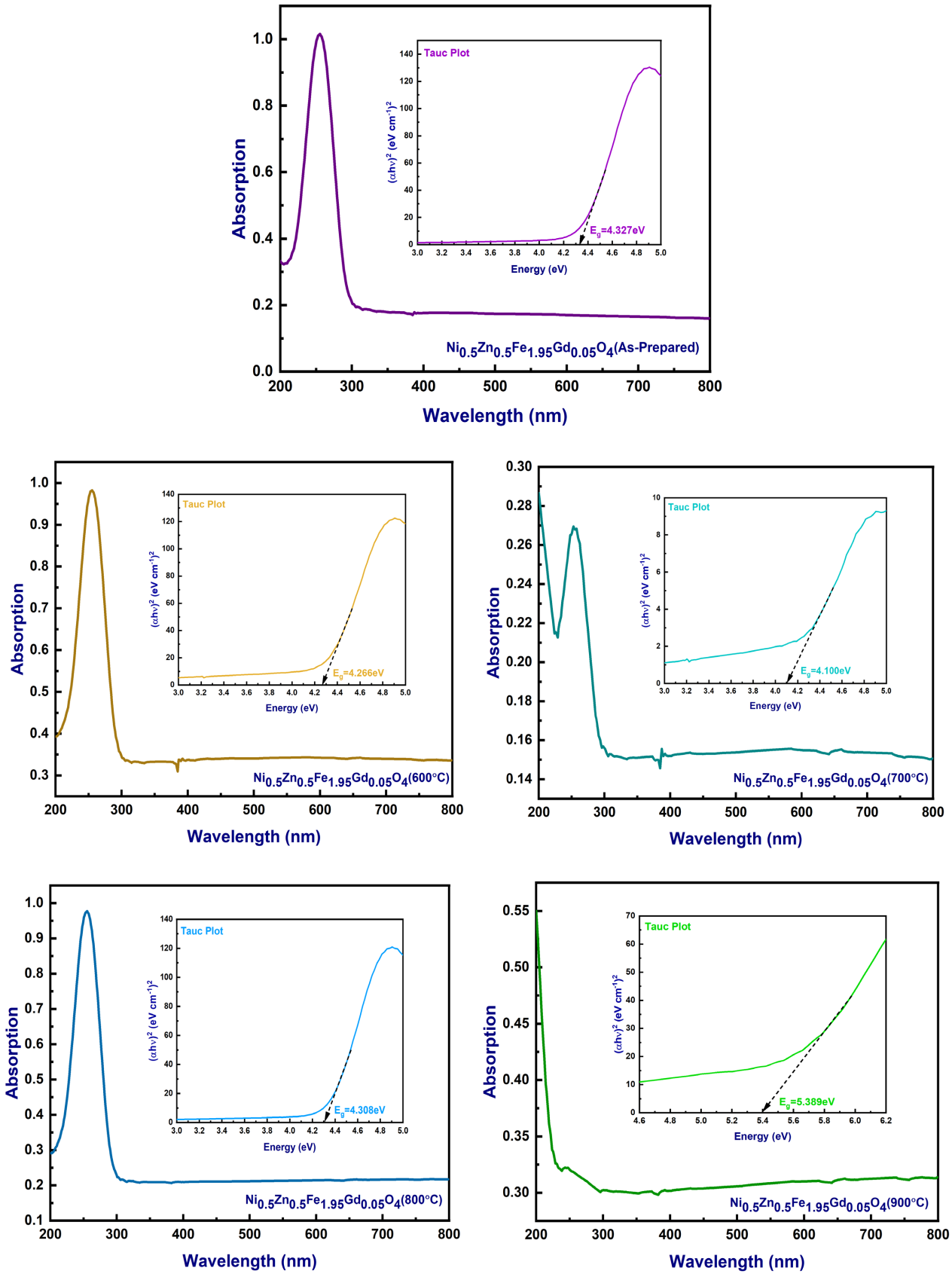

Figure 7. Tauc plots of $Ni_{0.5}Zn_{0.5}Gd_{0.05}Fe_{1.95}O_4$ ferrite nanoparticles (as-prepared and calcinated at 600˚C, 700˚C, 800˚C & 900˚C).

and

$$\alpha = \frac{2.303A}{t} \tag{13}$$

where, α is absorption coefficient, A is the absorbance, and t is the thickness of the samples. To calculate the optical absorption for the present ferrite nanoparticles, the following Tauc's relation (14) [33] [34] is used

$$(\alpha h\nu)^{1/n} = A\left(h\nu - E_g\right) \tag{14}$$

where, α is absorption coefficient, h is Plank's constant, ν is frequency; A is absorbance and E_g is optical energy bandgap. $(\alpha h\nu)^{1/n}$ was plotted as a function of the photon energy ($h\nu$) for different n values (n = 1/2, 3/2, 2, 3). These plots are known as Tauc plots [35] and are presented in **Figure 7**. For direct allowed transition n = 1/2, indirect allowed transition n = 2, direct forbidden transition n = 3/2 and forbidden indirect transition n = 3. To determine the possible transitions, $(\alpha h\nu_2)$ vs $h\nu$ is plotted and corresponding optical energy bandgap were obtained from extrapolating the straight portion of the graph on $h\nu$ axis. The optical energy bandgap obtained in the range of 4.100 to 5.389 eV. The sample calcinated at 700˚C exhibited minimum optical energy bandgap of 4.100 eV whereas the sample calcinated at 900˚C exhibited maximum optical energy bandgap of 5.389 eV. The energy gap can be attributed to the energy difference between conduction band and valence band. This may be due to presence of additional sub-band-gap energy levels that are induced by the abundant surface and interface defects in the agglomerated nanoparticles [36] [37].

4. Conclusions

It is evident that the effect of calcination temperature was present on all factors that are studied in this paper. Some of the salient conclusions:

1) The crystallite size was increased from 11.75 nm to 18.13 nm as the calcination temperature increased from 600˚C to 900˚C whereas as-prepared sample exhibited 17.61 nm.

2) The dislocation density was decreased from 7.243×10^{-3} to 3.042×10^{-3} nm^{-2} as the calcination temperature increased from 600˚C to 900˚C.

3) The micro strain was decreased from 10×10^{-4} to 6.452×10^{-4} as the calcination temperature increased from 600˚C to 900˚C.

4) The characteristic absorbance peaks were obtained at 255.2 nm for the ferrite nanoparticles of as-prepared and calcinated at 600˚C and 800˚C whereas it was obtained as 252.8 nm for the sample calcinated at 700˚C and there was no such characteristic peak in UV-visible range for the sample calcinated at 900˚C; it is expected in the below 200 nm region.

5) The optical energy gap was calculated using Kubelka-Munk equation based on Tauc's plot and found in the range 4.100 eV to 5.389 eV. The lowest energy gap of 4.100 eV exhibited by the sample calcinated at 700˚C and the highest energy gap of 5.389 eV by the sample calcinated at 900˚C.

6) It's evident that the tunable band gaps can be obtained with varying calcination temperature.

Acknowledgements

The author KVK expressed his thankfulness to the Registrar, JNTU Hyderabad for encouragement in carrying out this research work and extended his gratefulness to Dr. Ch. Shilpa Chakra for her constant support in bringing out the results in proper shape.

Conflicts of Interest

The author declares no conflicts of interest regarding the publication of this paper.

References

[1] Chandra Babu Naidu, K., Roopas Kiran, S. and Madhuri, W. (2017) Investigations on Transport, Impedance and Electromagnetic Interference Shielding Properties of Microwave Processed NiMg Ferrites. *Materials Research Bulletin*, **89**, 125-138. https://doi.org/10.1016/j.materresbull.2017.01.015

[2] Rajput, J.K., Arora, P., Kaur, G. and Kaur, M. (2015) $CuFe_2O_4$ Magnetic Heterogeneous Nanocatalyst: Low Power Sonochemical-Coprecipitation Preparation and Applications in Synthesis of 4H-Chromene-3-Carbonitrile Scaffolds. *Ultrasonics Sonochemistry*, **26**, 229-240. https://doi.org/10.1016/j.ultsonch.2015.01.008

[3] Srinivasan, S.Y., Paknikar, K.M., Bodas, D. and Gajbhiye, V. (2018) Applications of Cobalt Ferrite Nanoparticles in Biomedical Nanotechnology. *Nanomedicine*, **13**, 1221-1238. https://doi.org/10.2217/nnm-2017-0379

[4] Hankiewicz, J.H., Pajak, Z. and Murakhowski, A.A. (1991) Nuclear Magnetic Resonance in $Ba_3Co_2Fe_{24}O_{41}$ Ferrite. *Journal of Magnetism and Magnetic Materials*, **101**, 134-136. https://doi.org/10.1016/0304-8853(91)90704-E

[5] Mathpal, M.C., Niraula, G., Chand, M., Kumar, P., Singh, M.K., Sharma, S.K., *et al.* (2021) State of Art of Spinel Ferrites Enabled Humidity Sensors. In: *Spinel Nanoferrites*, Springer, Cham, 437-475. https://doi.org/10.1007/978-3-030-79960-1_14

[6] Kotnala, R.K. and Shah, J. (2016) Green Hydroelectrical Energy Source Based on Water Dissociation by Nanoporous Ferrite. *International Journal of Energy Research*, **40**, 1652-1661. https://doi.org/10.1002/er.3545

[7] Manikandan, V., Sikarwar, S., Yadav, B.C. and Mane, R.S. (2018) Fabrication of Tin Substituted Nickel Ferrite (Sn-NiFe2O4) Thin Film and Its Application as Opto-Electronic Humidity Sensor. *Sensors and Actuators A*: *Physical*, **272**, 267-273. https://doi.org/10.1016/j.sna.2018.01.059

[8] Yue, Q., Liu, C., Wan, Y., Wu, X., Zhang, X. and Du, P. (2018) Defect Engineering of Mesoporous Nickel Ferrite and Its Application for Highly Enhanced Water Oxidation Catalysis. *Journal of Catalysis*, **358**, 1-7. https://doi.org/10.1016/j.jcat.2017.10.027

[9] Yasmin, N., Inam, I., Malik, I.A., Zahid, M., Ashiq, M.N., Abdulsatar, S., *et al.* (2018) Structural and Magnetic Properties of Cr Doped Strontium Spinel Ferrite $SrFe_2O_4$ by Sol-Gel Auto-Combustion Method. *Physica B*: *Condensed Matter*, **550**, 90-95. https://doi.org/10.1016/j.physb.2018.08.039

[10] Gupta, M. and Randhawa, B.S. (2012) Microstructural, Magnetic and Electric Prop-

erties of Mixed Cs–Zn Ferrites Prepared by Solution Combustion Method. *Solid State Sciences*, **14**, 849-856. https://doi.org/10.1016/j.solidstatesciences.2012.04.010

[11] Haralkar, S.J., Kadam, R.H., More, S.S., Shirsath, S.E., Mane, M.L., Patil, S. and Mane, D.R. (2012) Substitutional Effect of Cr^{3+} Ions on the Properties of Mg–Zn Ferrite Nanoparticles. *Physica B*: *Condensed Matter*, **407**, 4338-4346. https://doi.org/10.1016/j.physb.2012.07.030

[12] Amaliya, A.P., Anand, S. and Pauline, S. (2018) Investigation on Structural, Electrical and Magnetic Properties of Titanium Substituted Cobalt Ferrite Nanocrystallites. *Journal of Magnetism and Magnetic Materials*, **467**, 14-28. https://doi.org/10.1016/j.jmmm.2018.07.058

[13] Pal, J. and Chauhan, P. (2010) Study of Physical Properties of Cobalt Oxide (CO_3O_4) Nanocrystals. *Materials Characterization*, **61**, 575-579. https://doi.org/10.1016/j.matchar.2010.02.017

[14] Hu, L., Wu, L., Liao, M., Hu, X. and Fang, X. (2012) Electrical Transport Properties of Large, Individual $NiCo_2O_4$ Nanoplates. *Advanced Functional Materials*, **22**, 998-1004. https://doi.org/10.1002/adfm.201102155

[15] Cui, B., Lin, H., Liu, Y.Z., Li, J.B., Sun, P., Zhao, X.C. and Liu, C.J. (2009) Photophysical and Photocatalytic Properties of Core-Ring Structured $NiCo_2O_4$ Nanoplatelets. *The Journal of Physical Chemistry C*, **113**, 14083-14087. https://doi.org/10.1021/jp900028t

[16] Yousef, T.A., El-Reash, G.A., Attia, M.I. and El-Tabai, M.N. (2015) Comparative Ligational, Optical Band Gap and Biological Studies on Cr (III) and Fe (III) Complexes of Hydrazones Derived from 2-hydrazinyl-2-oxo-N-phenylacetamide with Both Vanillin and *O*-Vanillin. *Chemical Physics Letters*, **636**, 180-192. https://doi.org/10.1016/j.cplett.2015.07.001

[17] Yousef, T.A., El-Reash, G.A., El-Gammal, O.A. and Bedier, R.A. (2012) Co (II), Cu (II), Cd (II), Fe (III) and U (VI) Complexes Containing a NSNO Donor Ligand: Synthesis, Characterization, Optical Band Gap, *in Vitro* Antimicrobial and DNA Cleavage Studies. *Journal of Molecular Structure*, **1029**, 149-160. https://doi.org/10.1016/j.molstruc.2012.06.050

[18] Melsheimer, J., Mahmoud, S.S., Mestl, G. and Schlögl, R. (1999) *In Situ* UV-VIS Diffuse Reflectance Spectroscopy of Reduction-Reoxidation of Heteropoly Compounds by Methanol and Ethanol: A Correlation between Spectroscopic and Catalytic Data. *Catalysis Letters*, **60**, 103-111. https://doi.org/10.1023/A:1019094621316

[19] K Rama, K., K Vijaya, K. and Dachepalli, R. (2012) Structural and Electrical Conductivity Studies in Nickel-Zinc Ferrite. *Advances in Materials Physics and Chemistry*, **2**, 185-191. https://doi.org/10.4236/ampc.2012.23028

[20] Berchmans, L.J., Selvan, R.K. and Augustin, C.O. (2004) Evaluation of Mg^{2+}-Substituted $NiFe_2O_4$ as a Green Anode Material. *Materials Letters*, **58**, 1928-1933. https://doi.org/10.1016/j.matlet.2003.12.008

[21] Yue, Z., Zhou, J., Li, L., Wang, X. and Gui, Z. (2001) Effect of Copper on the Electromagnetic Properties of Mg-Zn-Cu Ferrites Prepared by Sol-Gel Auto-Combustion Method. *Materials Science and Engineering*: *B*, **86**, 64-69. https://doi.org/10.1016/S0921-5107(01)00660-2

[22] Kumar, K.V., Bhavani, S.D. and Shukur, M.A. (2022) The Study of Temperature Dependent Structural and Elastic Properties of. *Bulgarian Journal of Physics*, **20**, 1-16.

[23] Pawar, D.K., Pawar, S.M., Patil, P.S. and Kolekar, S.S. (2011) Synthesis of Nanocrystalline Nickel–Zinc Ferrite ($Ni_{0.8}Zn_{0.2}Fe_2O_4$) Thin Films by Chemical Bath De-

position Method. *Journal of Alloys and Compounds*, **509**, 3587-3591. https://doi.org/10.1016/j.jallcom.2010.12.079

[24] Thanh, N.K., Loan, T.T., Anh, L.N., Duong, N.P., Soontaranon, S., Thammajak, N. and Hien, T.D. (2016) Cation Distribution in $CuFe_2O_4$ Nanoparticles: Effects of Ni Doping on Magnetic Properties. *Journal of Applied Physics*, **120**, Article ID: 142115. https://doi.org/10.1063/1.4961722

[25] Chopra, K.L. (1969) Thin Film Phenomena. McGraw-Hill, New York, 196.

[26] Naresh, U., Kumar, R.J. and Parasad, T.R. (2018) Optical Properties of Copper Ferrite Nano-Particle Synthesized via Hydrothermal Technique. *Bulletin of Pure & Applied Sciences-Physics*, **37**, 172-177. https://doi.org/10.5958/2320-3218.2018.00024.6

[27] Xue, S.W., Zu, X.T., Zhou, W.L., Deng, H.X., Xiang, X., Zhang, L. and Deng, H. (2008) Effects of Post-Thermal Annealing on the Optical Constants of ZnO Thin Film. *Journal of Alloys and Compounds*, **448**, 21-26. https://doi.org/10.1016/j.jallcom.2006.10.076

[28] Ashour, A., El-Kadry, N. and Mahmoud, S.A. (1995) On the Electrical and Optical Properties of CdS Films Thermally Deposited by a modified Source. *Thin Solid Films*, **269**, 117-120. https://doi.org/10.1016/0040-6090(95)06868-6

[29] Greenaway, D.L. and Harbeke, G. (1968) Optical Properties and Band Structure of Semiconductors. Pergamon, New York.

[30] Güneri, E. and Kariper, A. (2012) Optical Properties of Amorphous CuS Thin Films Deposited Chemically at Different pH Values. *Journal of Alloys and Compounds*, **516**, 20-26. https://doi.org/10.1016/j.jallcom.2011.11.054

[31] Pathan, H.M., Desai, J.D. and Lokhande, C.D. (2002) Modified Chemical Deposition and Physico-Chemical Properties of Copper Sulphide (Cu2S) Thin Films. *Applied Surface Science*, **202**, 47-56. https://doi.org/10.1016/S0169-4332(02)00843-7

[32] Srivastava, M., Ojha, A.K., Chaubey, S. and Materny, A. (2009) Synthesis and Optical Characterization of Nanocrystalline $NiFe_2O_4$ Structures. *Journal of Alloys and Compounds*, **481**, 515-519. https://doi.org/10.1016/j.jallcom.2009.03.027

[33] Tauc, J. (Ed.). (2012) Amorphous and Liquid Semiconductors. Springer Science & Business Media, Berlin.

[34] Tauc, J., Grigorovici, R. and Vancu, A. (1966) Optical Properties and Electronic Structure of Amorphous Germanium. *Physica Status Solidi* (*B*), **15**, 627-637. https://doi.org/10.1002/pssb.19660150224

[35] Orhan, N. and Baykul, M.C. (2012) Characterization of Size-Controlled ZnO Nanorods Produced by Electrochemical Deposition Technique. *Solid-State Electronics*, **78**, 147-150. https://doi.org/10.1016/j.sse.2012.05.051

[36] Kislov, N., Srinivasan, S.S., Emirov, Y. and Stefanakos, E.K. (2008) Optical Absorption Red and Blue Shifts in $ZnFe_2O_4$ Nanoparticles. *Materials Science and Engineering*: *B*, **153**, 70-77. https://doi.org/10.1016/j.mseb.2008.10.032

[37] Kale, R.B. and Lokhande, C.D. (2004) Influence of Air Annealing on the Structural, Optical and Electrical Properties of Chemically Deposited CdSe Nano-Crystallites. *Applied Surface Science*, **223**, 343-351. https://doi.org/10.1016/j.apsusc.2003.09.022